Interaction of SH guided waves with wall thinning

Alan C. Kubrusly, Miguel A. Freitas, Jean Pierre von der Weid, Steve Dixon

Abstract—**This paper investigates through experiment and finite element modelling, the interaction and mode conversion phenomenon of SH0 and SH1 guided wave modes on a metal plate with machined wall thinning. Quantitative analysis was performed by calculating the reflection and transmission coefficients at the leading and trailing linearly tapered edges, for incident SH0 and SH1 modes. Several geometries were evaluated by varying the taper length and depth. Experiments were performed with periodic permanent magnet array EMATs as transmitters and receivers, generating a single SH mode, whilst both SH0 and SH1 are received. Experimental and numerical data show good agreement, revealing that the interaction of SH guided waves with such defects is complex when mode conversion arises. The values of the reflection and transmission coefficients are non-monotonic along the thinning depth and edge angle ranges. The quantitative results provide insight into the capabilities and limitations of guided SH wave measurements for simple corrosion type defects, indicating that with current capabilities, inspection of real defects will be limited to screening type measurements rather than detailed quantification of the defect region.**

Keywords—SH guided waves, mode conversion, PPM EMAT, wall thinning defects, reflection and transmission coefficients.

1. Introduction

The use of Shear Horizontal (SH) guided waves for non-destructive evaluation of plates and pipes to detect defects such as cracks and corrosion has been extensively reported in the literature [1-9]. In laboratory tests, notches and machined wall thinning sections are

1

26   commonly used as a first step approximation of a corrosion type defect [10-16]. According to

27   the working frequency, two regimes of operation are commonly defined, namely low and

28   high frequency-thickness regimes [15-17]. In the latter, the operating frequency range

29   encompasses more than one mode. Otherwise, when the operating frequency only allows the

30   fundamental, SH0, mode to propagate, one operates in the low frequency-thickness regime.

31   In both regimes, the interaction of the SH guided waves with the thinning regions, such as

32   corrosion-like defects, depends on the thinning geometry [2, 10-13, 18, 19]. There is,

33   however, an underlying difference in what concerns mode conversion in both regimes. In the

34   low-frequency regime, when the incoming mode impinges upon a lower thickness region it is

35   scattered and transmitted to this region without having its energy shared between other

36   propagating modes [2, 11, 13, 20, 21], whilst in the high-frequency there may be mode

37   conversion to other propagating modes either in reflection or transmission when interacting

38   with defects [9, 14, 18, 19, 22]. There are of course instances where the original sample

39   thickness is such that higher order modes than the SH1 mode can propagate, but for most

40   typical sample thicknesses and EMAT wavelengths, one is usually only considering cases

41   where the original plate thickness only supports SH0 and SH1 modes, and we will limit our

42   discussion to consideration of the interaction of just these two modes with wall thinning

43   defects in this paper.

44   Interest in the interaction of SH waves with discontinuities in the high frequency-thickness

45   regime goes back decades, where Koshiba et al. [22] proposed an analytical approach

46   combined with finite element method to analyse the scattering of SH waves in plates. Ditri

47   [23] analytically studied the scattering of SH waves in plate's discontinuities either as

48   thickness reduction or different materials. Recently, Pau et al. [15, 16] quantitatively analysed

49   the reflection and transmission coefficients for incident SH0 waves in plates with abrupt

50   thickness reduction. Pau used an analytical model based on the reciprocity principle in order

2

51 to evaluate the coefficients, using only finite element simulations without experimental

52 validation.

53   Interaction of SH guided waves in gradual thickness change was also analysed since it

54 represents a more relevant corrosion path geometry than discontinuities. Nurmalia et al. [18]

55 experimentally investigated SH guided waves in plates, and later torsional guided waves in

56 pipes [19], with thickness reduction at tapered edges, in few different edge angles, focusing

57 on the case where the defective area presents a remaining thickness below the SH1 cut-off

58 thickness and showed that interaction depends on the taper length. When an SH mode

59 impinges upon the defect edge, part of it is reflected and part is transmitted to the defective

60 area. The scattered wave suffers partial mode conversion, being distributed between SH0 and

61 SH1 modes. The same effect is observed when the guided waves leave the defect region, into

62 the thicker area. For abrupt defects there is strong mode conversion in both edges. For very

63 long tapers it was observed the phenomenon of total transmission of the SH0 mode into and

64 out of the defect and total reflection of SH1, without significant mode conversion in either

65 case. Interesting applications of total transmission of the fundamental mode and total

66 reflection of higher order modes through gradual tapers were proposed elsewhere. Kwon et

67 al. developed a thick waveguide transducer able to generate exclusively the SH0 mode [24]

68 and also performed pipe inspection using only the fundamental torsional mode even in the

69 high-frequency regime [7, 8]. Chen et al. [25] developed a unidirectional transmission device

70 for the SH1 mode.

71   Qualitative pipe inspection for corrosion at the high-frequency regime has been performed

72 using circumferential SH guided waves [3, 9] and torsional guided waves [26]. The basic

73 concept consists of a screening system that transmits and receives the SH0 and SH1 modes

74 using PPM EMATs. The presence of the defect introduces changes in the received signal,

75 enabling defect identification by comparative change in the scan appearance compared to a

3

76   clear pipe section appearance. Apart from signal amplitude changes, phase changes also

77   suggested the presence of a defect due to the different propagating speeds of these modes,

78   and the speed dependence with thickness for the dispersive SH1 mode.

79   Since real corrosion defect can present varied thickness profiles [13, 20, 21], the analysis

80   of tapered wall thinning models is a relevant intermediate step to evaluate corrosion-like

81   defects. The preliminary study on this type of geometry revealed that not only the depth but

82   also the taper angle influence the behaviour of SH guided waves. This fact appeals for a more

83   deep investigation on the interaction and mode conversion of SH guided wave.

84   Understanding the amount of reflection and transmission and the degree of mode conversion,

85   as a function of the thinning depth and taper angle is, therefore, crucial for gaining the

86   knowledge required to interpret data and finally establish an inspection procedure that is able

87   to provide quantitative information about a real corrosion defect or assess the inherent

88   limitations and difficulties on the use of SH guided waves for detail defect profiling.

89   Although the aforementioned previous work has presented a helpful overview of the

90   phenomenon of the interaction of SH guided waves in the high-frequency regime with

91   tapered thinning regions, particularly [18] and [19], there is still the lack of quantitative data

92   for a comprehensive range of defect depths and edge taper angles. That is, few edge angle

93   and depth were analysed and a complete delineation of the mode conversion behaviour is still

94   unaccomplished. We address this in this paper by calculating the coefficients for reflection

95   and transmission in the leading and trailing edges of a wall thickness region with different

96   depths and edge angles, for both mode-converted and non-converted modes. The fundamental

97   (SH0) and first-order shear horizontal (SH1) guided wave modes are individually generated

98   and both of them are separately received in each generation case. Numerical and

99   experimental analysis is presented for plates with a machined thinner region to simulate wall

100 loss through corrosion.

2. SH guided waves and PPM EMAT

Shear horizontal guided waves have displacement perpendicular to the propagation direction and parallel to the plate's surface. Apart from the fundamental zero-order SH0 mode, all other higher order modes are dispersive, which means that the phase and group velocity are frequency dependent. The phase velocity is given by:

$$c = 2c_T f h \,/\sqrt{4f^2 h^2 - n^2 c_T^2} \,, \tag{1}$$

where n is the mode order, c_T the shear wave speed, f the frequency and h the plate thickness [27]. Non-fundamental modes are only able to propagate for a frequency-thickness product above a cut-off value. Therefore, at a fixed frequency, higher order modes cannot propagate if the plate's thickness is below the cut-off thickness given by

$$h_{\text{cut-off}} = n \, c_T / 2f \,. \tag{2}$$

SH guided waves present advantages such as simple dispersion curves and no energy-leakage to a fluid in contact with the sample surface, making them attractive for pipeline inspection [3, 9, 26]. SH guided waves can be generated and detected with periodic permanent magnet array (PPM) EMATs, which consist of an array of magnets with an elongated spiral coil underneath [28, 29]. The spacing or pitch of the magnets in the PPM EMATs imposes a nominal wavelength on the generated waves. However, due to the finite number of magnets in the array, the EMAT has a wavelength bandwidth of waves that can be excited [29, 30]. Together with the frequency bandwidth of the excitation electric current applied to the coil, a region of operation in which SH waves can be generated or receiver is defined. In order to visualize the operating region it is convenient to plot it together with the dispersion curve, if the operating region crosses the dispersion curve of one mode then this one is generated and received predominantly. Fig 1 shows the SH dispersion curves for an 8mm aluminium plate, according to Eq. (1), superposed on to the operating region of a 3

125 cycle 10mm PPM EMAT, driven by an 8 cycle tone burst current pulse at 311 kHz, plotted in

126 the frequency-phase speed plane. The higher intensity of the operating region indicates the

127 excitation efficiency when mapped on to the dispersion curves. In the example below, there

128 would be efficient excitation of the SH0 mode between roughly 290 kHz – 330 kHz, with a

129 less efficient excitation of the SH1 mode at approximately 340 kHz.
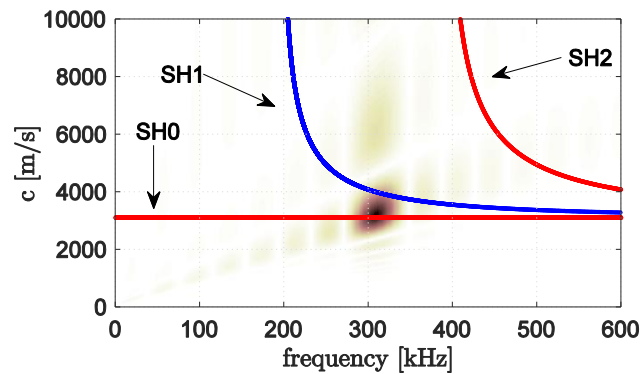
130

131 Fig.1. SH modes phase speed dispersion curves superposed to the probe operating region for SH0 excitation.

132 **3. Finite element investigation**

133 *3.1. Numerical procedure and geometry*

134 Numerical analysis was performed for an 8 mm aluminium plate using a commercial,

135 time-domain, Finite Element Method (FEM) solver, PZFlex[©]. The aluminium density and

136 transverse wave speed used in the model were set to 2698 kg/m^3 and c_T =3111 m/s,

137 respectively. The geometry is shown in Fig. 2: the plate's plane lies in the *x-y* plane

138 (thickness in the *y* direction, length in the *x* direction), the chosen solver allows simulation of

139 SH waves in a two-dimensional model without the need of modelling the direction of particle

140 displacement, along the plate's width, in the *z* direction. The model effectively treats the *z*

141 direction as infinite and in the experimental geometry used, this is a reasonable

142 approximation. Both ends of the plate are terminated with PZFlex[©]'s built-in absorbing

143 boundary conditions to avoid reflections. A tapered thinner defect is modelled starting at 182

6

144   mm with a total length of 150 mm. Depth, d, and edge angle, α, of the thinned region were

145   varied in order to analyse the behaviour as a function of the taper angle and the depth of

146   thinned region. The linear taper can be described either by its angle or by its length, which is

147   related to the angle by

148    $$\ell = d\,cot(\alpha)\,. \tag{3}$$

149   The adopted defect total length is long enough so that the reflection from both ends do not

150   mix in the time domain signal, so that there is no interference phenomenon on the coefficients

151   (as addressed elsewhere [2, 10-13, 15, 16, 21]). Here only the geometrical effect on the

152   coefficients is analysed.

153
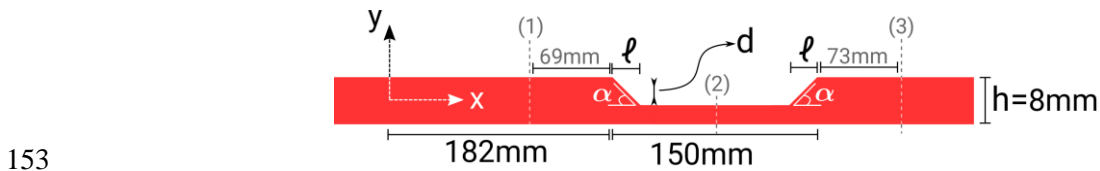
154   Fig.2.Plate and defect geometry.

155   The SH wave is generated by imposing a spatial force profile that mimics the PPM EMAT

156   induced forces in the specimen surface. This was performed by applying forces at the nodes

157   on the surface of the model along the z-direction according to the following equation:

158    $$f[i] = sin(2\pi x[i]/\lambda),\, -N\lambda/2 \le x[i] \le N\lambda/2\,, \tag{4}$$

159   where $f[i]$ is the applied force toward z direction at node i whose longitudinal position at the

160   surface is $x[i]$, λ is the wavelength, and N the number of spatial cycles. Following Eq. (4),

161   with $N = 3$ and $\lambda = 10$mm, the PPM EMAT induced force distribution is approximately

162   simulated without the need of including the EMAT in the model. This approach was adopted

163   and validated previously elsewhere [3, 28, 29, 31]. The applied forces were varied in time

164   following an excitation signal consisting of an 8 cycle tone burst with a centre frequency of

165   either 311 kHz or 367 kHz, according to the intended mode to be generated, the SH0 or the

166   SH1 mode respectively. In this paper, the operating region, formed by the EMAT spatial

167   distribution and time-varying excitation signal used in the numerical model or applied to the

168   amplifying electronics, in the experiment, is set wide enough both in the frequency and in the

169   wavelength ranges, so that mode conversion between the SH0 and SH1 modes can be

170   detected with a conventional PPM EMAT, with approximately similar sensitivity; as can be

171   seen in Fig. 1 the operating region encompasses the two modes' dispersion curves. Single

172   mode excitation and separation of possible mode-converted waves are then ensured by

173   adopting the dual transmission and receiving technique proposed in [29].

174   Fig. 3 (a) shows the particle velocity contour plot for a plate with a 3 mm defect at 50°

175   edges, equivalent to a taper of about one quarter wavelength, for an SH0 incident mode. One

176   can observe the reflections at approximately 50 mm and the transmission out of the far end of

177   the defect at approximately 350 mm. Before and after the thinner region one can see that

178   both, SH0 and SH1 modes, are mixed [28]. The technique proposed in [29] allows separation

179   between the symmetric and antisymmetric parts of the received signals at the surfaces. It can,

180   however, be extended for all of the plate cross section, allowing separation of waves profile

181   across the thickness. These parts are shown in Fig. 3 (b) and (c), respectively, where one can

182   clearly identify the presence of the symmetric SH0 and anti-symmetric SH1 at the same

183   position, both before and after the defect. A very low amplitude SH1 mode is seen inside the

184   thinner region, between 200 and 250 mm in Fig. 3 (c).
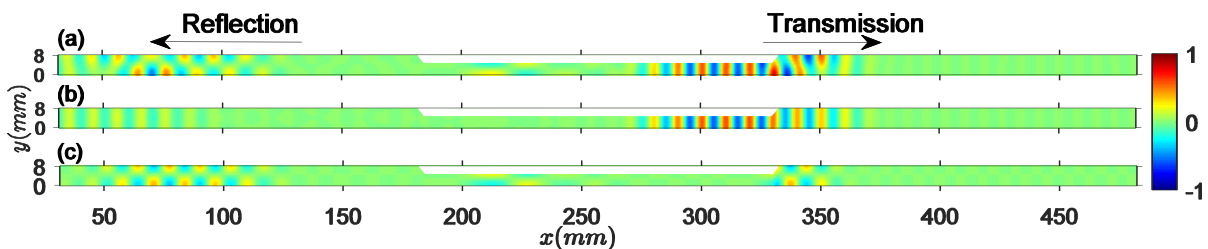
186   Fig.3. Normalized particle velocity for a plate with 3 mm defect at 50° edges at 116μs (a), symmetric
187   component (b) and antisymmetric component (c).

188   Quantitative analysis was carried by calculating the coefficients for reflection at the defect

189   region edge, R_{ij}, transmission to the region, T_{ij} and transmission out of the region far end of

190   the region, TT_{ij}. The subscript i and j in the coefficient notation represents the generated and

191   received mode orders, respectively. These coefficients can be formally defined by

$$R_{ij} = \frac{A_j^{(1)-}}{A_i^{(1)+}} \; , \qquad\qquad (5a)$$

$$T_{ij} = \frac{A_j^{(2)+}}{A_i^{(1)+}} \sqrt{\frac{h-d}{h}} \; , \qquad\qquad (5b)$$

$$TT_{ij} = \frac{A_j^{(3)+}}{A_i^{(1)+}} \; , \qquad\qquad (5c)$$

195   where A is the maximum peak-to-peak amplitude of the received signal, the superscripts +

196   and - mean the forward and backward propagating waves, respectively. The superscripts (1),

197   (2) and (3) indicate the reading positions: before the defect, on the defect and after the far end

198   of the defect, respectively, as shown in Fig. 2. Due to the operating region, i and j can be 0 or

199   1 here, corresponding to the SH0 or SH1 modes, respectively. All coefficients are related to

200   the incident wave, $A_i^{(1)+}$. It is worth highlighting that both the SH0 and SH1 modes inside the

201   thinned region can contribute to TT_{ij} coefficients when a single mode is incident on the

202   thinned region's leading edge. For instance, when the SH0 mode is generated, it is

203   transmitted to the thinned region either as the SH0 mode or as the SH1 mode, giving rise to

204   T_{00} and T_{01}, respectively. Both modes then propagate in the thinned region independently and

205   when they interact with the trailing edge a new mode conversion can occur. Therefore, the

206   SH0 or the SH1 modes transmitted out of the region can be originated from either the SH0 or

207   SH1 modes in the thinned region, even when only one single mode, either the SH0 or SH1

208   mode, is generated. The following schematic illustrates the possibilities for SH0 and SH1

209   modes transmitted away from the region due to the incident SH0 on the region's leading

210   edge:

$$SH0 \to \begin{cases} SH0 \to \begin{cases} SH0 & (a) \\ SH1 & (b) \end{cases} \\ SH1 \to \begin{cases} SH0 & (c) \\ SH1 & (d) \end{cases} \end{cases} \quad , \tag{6}$$

212   where the first arrow represents the transmission to the region and the second, the

213   transmission out of the region's far end. The SH0 mode that propagates away from the defect

214   can arise from either case (a) or case (c) which are not, necessarily, clearly separated in time.

215   This, however, only holds when the region remaining thickness is above the SH1 mode cut-

216   off thickness, otherwise cases (c) and (d) are no longer possible. A similar argument applies

217   to the SH1 modes that are transmitted from the end of the thinned region. Therefore, here

218   only one coefficient for the transmission out of the region, TT_{ij}, is calculated, which consist

219   of the two possibilities for the propagating modes inside the region. Strictly speaking, TT_{ij} is

220   not a real transmission coefficient, (whereas T_{ij} and R_{ij} are real) but rather is a useful figure of

221   merit to quantitatively interpret the interaction phenomenon throughout a thinned region. This

222   is done because in practical measurements it is typically the maximum signal amplitude that

223   is the clearest observable parameter.

224   In order to calculate the coefficients, a time gate in which the forward or backward waves

225   are expected to arrive was defined for the SH0 and SH1 signals according to the receiving

226   position, tone burst time duration and group speed of the modes. It is worth noting that the

227   group speed is different not only when mode conversion occurs, but also when SH1

228   propagates inside the thinner regions since it is dispersive. Some additional remarks on the

229   coefficient calculation are necessary. The square root in Eq. (3b) is included to compensate

230   the natural energy increase of a wave when it is transmitted into a thinner region of the plate

231   without loss. When the thinned region remaining thickness is below the SH1 cut-off

232 thickness, its group speed is not a real number and thus a time gate for T_{i1} cannot be defined.

233 In this case, no time gate restriction is applied and the whole antisymmetric signal on the

234 region is considered to calculate the T_{i1} coefficient. This was done in order to allow analysis

235 of any residual antisymmetric component inside the defect when the cut-off thickness is

236 exceeded.

237   The time gates and signals for a plate with a 2 mm deep thinner region (25% of thickness

238 reduction) at 55° edges are shown in Fig. 4 for SH1 generation at 367 kHz, for the three

239 receiver positions. The reflected SH1 and SH0 modes are seen in Figs. 4 (a) and (b),

240 respectively. The transmission to the thinned region is shown in Figs. 4 (c) and (d), for the

241 SH1 and SH0 modes, respectively. Finally, Figs. 4 (e) and (f) show the SH1 and SH0 modes,

242 respectively, transmitted out of the far end of the thinned region.
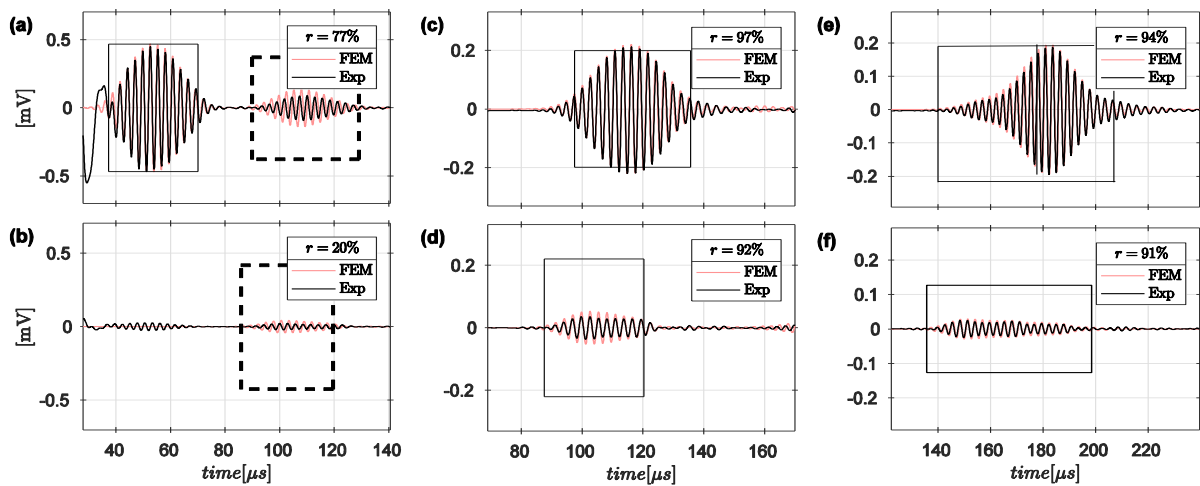
244 Fig.4. Experimental (black) and simulation (red) signals for SH1 generated at 367 kHz in a plate with 2mm
245 (25% of thickness reduction) defect at 55° edges, received before the defect (a and b), on the defect (c and d)
246 and after the defect (e and f). Continuous and dashed rectangles represent the theoretical arrival times of the
247 direct and reflected waves, respectively. Non-mode converted signals (a, c and e), mode converted signals (b, d
248 and f). The cross-correlation coefficients, r, between experimental and simulated signals are shown on the top of
249 each legend.

11

3.2. Coefficients for incident SH0 mode

251   Figure 5 shows the coefficients, R_{00}, R_{01}, T_{00}, T_{01}, TT_{00} and TT_{01} as a function of the

252   relative depth of the thinner region, *d/h*, and the taper length per wavelength. Firstly, it is

253   noticeable that the interaction is very dependent on the taper length. Note that in Fig. 5 (a)

254   and (b) there is an oscillatory pattern for R_{00} and R_{01}, respectively, for some simulated defect

255   depths. One can see that quasi-regular variations in the reflection coefficients, R_{00} and R_{01},

256   appear for high defect depths, deeper than 75% of thickness reduction, and also at very low

257   depths, of less than 25% of thickness reduction (more clearly shown in Figs. 9 and 10). This

258   behaviour is similar to the one reported by Carandente et al. [13] for the SH0 mode

259   impinging upon a tapered step-down defect in the low-frequency thickness regime. For

260   intermediate depths, the reflection coefficient decreases in a less complex manner, as the

261   taper length increases. The mode-converted reflection, R_{01}, between one quarter and half

262   wavelength is very intense whereas the non-mode converted, R_{00}, is very low.

263   The coefficient T_{00}, shown in Fig. 5 (c), is close to unity for long tapers, regardless of the

264   defect depth, whereas it decreases as the depth increases for abrupt edges. The coefficient

265   T_{01}, Fig. 5 (d), tends to increase with defect depth until the cut-off thickness is reached, then

266   it decreases to zero, as expected. For guided SH waves at 311 kHz, the cut-off thickness is 5

267   mm in aluminium, which corresponds to a defect depth of 3 mm, or 38% of thickness

268   reduction, in the 8 mm thick plate. However, one may observe that between 38% and 50%

269   defect depth, T_{01} is non-zero. This happens because the pulse bandwidth is finite, allowing

270   frequency components whose cut-off thickness has not been yet exceeded, to pass through the

271   thinned region. As the remaining thickness decreases, T_{01} eventually vanishes. The

272   coefficient TT_{00}, Fig. 5 (e), behaves similarly to T_{00}. It shows values close to unity for long

273   edges, when the taper length is more than two wavelengths. The coefficient TT_{01}, for more

274   abrupt edges, is maximum for defect depth of approximately half of the plate's original

thickness, as shown in Fig. 5 (f); its maximum value is about 80% for taper length less than

one half of the wavelength.
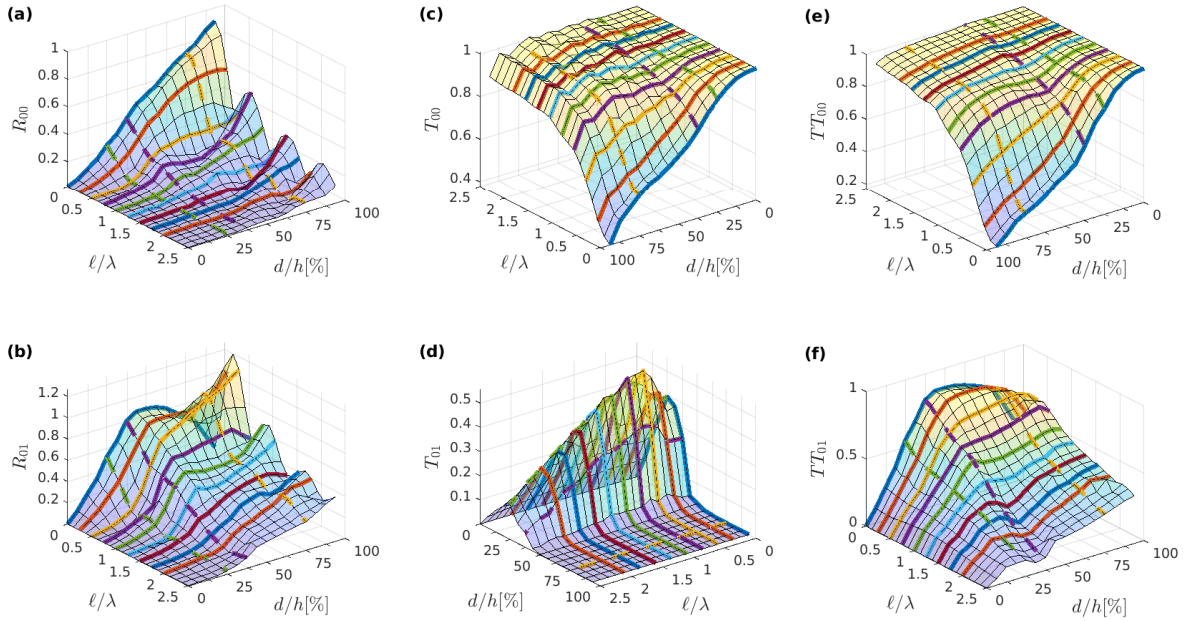
Fig.5. Coefficient due to SH0 generation as a function of defect depth and taper length. Continuous lines
represent taper length at multiples of one quarter wavelength, dashed lines represent defect depths of 25%, 38%
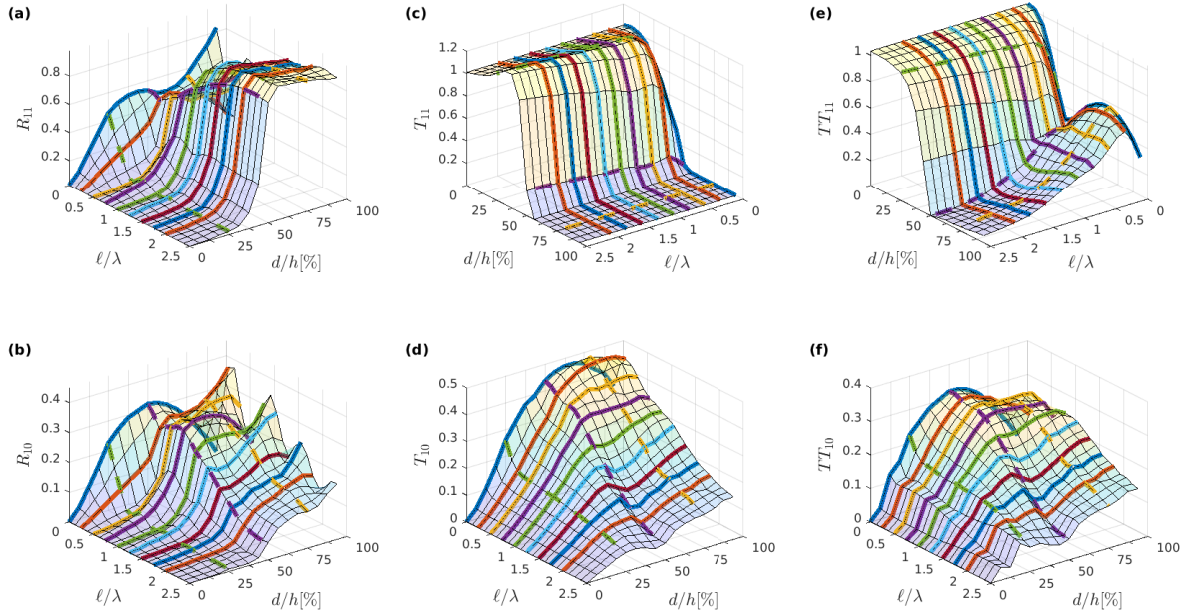(corresponding to remaining thickness equal to the cut-off thickness for the SH1 mode) and 75%.

3.3. Coefficients for incident SH1 mode

Figure 6 shows the coefficients as a function of the relative depth of the thinner region and

the taper length per wavelength when the SH1 mode is generated. Coefficients R_{11} and R_{10},

shown in Fig. 6 (a) and (b) respectively, exhibit more variation along the depth and taper

length axes. The oscillatory pattern for shallow defects is quite similar to the case in which

the SH0 is generated. However, for deep defects, the oscillation is not clearly exhibited, and

it is only observed in R_{10} for very deep defects, with d/h > 88%. For gradually tapered edges,

two very clear characteristics are observable in R_{11}: for shallow defects, when the cut-off

thickness is not exceeded (which is 4.2 mm at 367 kHz, corresponding to 3.8 mm depth, or

48% of thickness reduction), R_{11} is close to zero, whilst for deep defects, it is almost unity.

13

291   Detailed graphs for defect depths of 25%, 75% and 88% of plate thickness are shown in Figs.

292   12 to 14.

293   Fig. 6 (e) shows that the coefficient TT_{11} also has two distinct regions, when the remaining

294   thickness is above and below the SH1 cut-off thickness. For smaller defect depths, TT_{11}

295   decreases as the depth increases, with dependence on the taper length only between zero and

296   one half of the wavelength. This behaviour is very similar to T_{11}, suggesting that the

297   influence of the SH1 mode inside the defect is dominant for the case when the SH1 mode is

298   transmitted out of the defect. When the remaining thickness goes below the cut-off thickness,

299   the SH1 mode that arises after the defect is due to mode conversion from the SH0 inside the

300   defect. In this case, TT_{11} decreases as the taper length increases, since for very long tapers

301   there is almost total reflection for the SH1 mode as seen in Fig. 6 (a), and a very low

302   amplitude mode-converted SH0 wave transmitted to the thinned region, as seen in Fig. 6 (d).

303   TT_{10}, Fig. 6 (f), exhibits similar behaviour to T_{10}. It is also interesting to note that, generally,

304   there is more mode conversion in reflection and transmission when the SH0 mode is

305   generated, than when the SH1 mode is generated, as is clear in a comparison of the values of

306   R_{01} with R_{10}, and TT_{01} with TT_{10} in Figs. 5 and 6

307

14

Fig.6. Coefficient due to SH1 generation as a function of defect depth and taper length. Continuous lines represent taper length at multiples of one quarter wavelength, dashed lines represent defect depths of 25%, 50% (corresponding to remaining thickness equal to the cut-off thickness for the SH1 mode) and 75%.

The coefficient T_{11}, shown in Fig. 6 (c), is unity for small defect depths, showing that there is almost total transmission of SH1 into the defect. The behaviour along the taper length is approximately constant for tapers longer than one half of the wavelength, exhibiting some changes in T_{11} below this taper length. When the cut-off thickness is exceeded, T_{11} is effectively zero, as expected. There is maximum transmission of the mode converted SH0 mode to the thinner region, T_{10}, for a taper length of approximately one quarter wavelength, as observed in Fig. 6 (d), at a defect depth of approximately 75%. As the taper length increases, T_{10} decreases for all depths.

4. Experimental validation

Experiments were performed using a RITEC ® RPR-4000 Pulser/Receiver to generate and receive the signals from PPM EMATs used as transmitter and receiver. The excitation pulse was set to an 8 cycle tone burst at 311 kHz and 367 kHz to generate SH0 and SH1 modes respectively, as in the finite element simulations. After passing through the internal amplifier,

325 the received signal was acquired by an oscilloscope, with the driver and oscilloscope being

326 connected to a PC to automate data acquisition. Both emitter and receiver EMATs were 3

327 cycle 10 mm nominal wavelength PPM EMATs from Sonemat Ltd. The test sample was an 8

328 mm thick, 800 mm long and 250 mm wide aluminium plate. Four plates with different defect

329 angles were machined, at 10°, 45°, 55°, and 90°. For each angle, a thinning region with depth

330 from 1 mm down to 7 mm was machined in 1 mm steps. For each plate, machining started in

331 the shallowest depth, the experiment was performed, and then the same plate was remachined

332 to the next depth. Additional angles at 6 mm depth (25°, 30° and 35°) and 7 mm depth (25°,

333 30° and 65°) were also machined for further experimentation.

334   Dual excitation and reception on the upper and lower surfaces was adopted in order to

335 ensure single mode generation and to separate modes due to mode conversion following a

336 procedure described previously [29]. Fig. 7 shows the experimental setup. Experimental and

337 numerical signals are shown for a plate with a machined defect region with 25% of plate

338 thickness deep at 55° in Fig. 4 for generation of the SH1 mode, received at the three

339 positions. Numerical and experimental signals show good agreement. The cross-correlation

340 coefficient between the numerical and experimental signals shown in Fig. 4 was calculated

341 and presented in the legend of each plot. The worst values were obtained at position (1), 77%

342 for non-mode converted and 20% for mode-converted. The former is due to the interference

343 of the high voltage excitation pulse, used in the experiment, on the direct path received

344 signal, which can be seen around 40 μs in Fig.4(a). The latter is due to the inherent

345 imprecision on the experimental mode selectivity procedure for the mode-converted signal,

346 which does not completely eliminate the direct pulse, around 50 μs in Fig.4(b); a careful

347 analysis of the experimental precision of the mode selection procedure is addressed in [29].

348 Nevertheless, if one considers only the signal part inside the dashed rectangles in Fig.4(a) and

349 (b), corresponding to the waves reflected at the defect leading edge, then the cross-correlation

350 coefficient is 93% in both cases. All other signals present high correlation coefficient, above

351 90%. The good agreement also confirms the effectiveness of the finite element simulations.
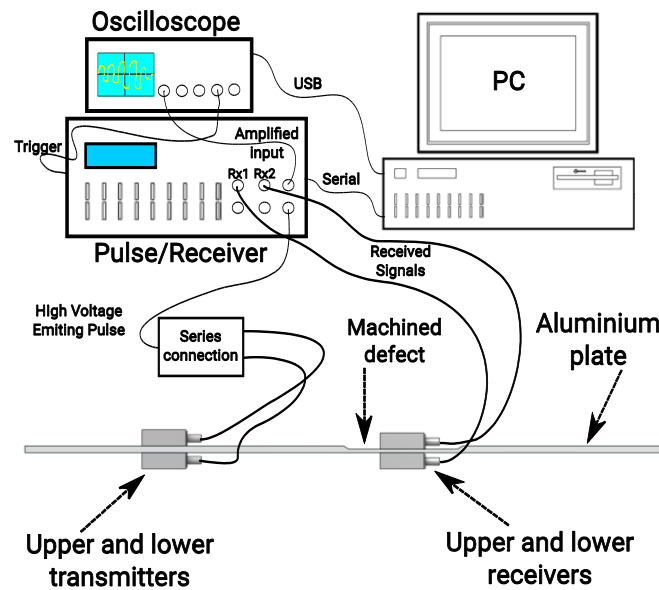
352

353 Fig.7. Experimental setup.

354   In order to calculate the experimental coefficients, one has to compensate for attenuation

355 of the experimental signals. The experimental attenuation coefficient was calculated by

356 measuring the received signals in several positions in a non-defective plate. This was done

357 for generating both SH0 and SH1 modes. One must also consider the wavelength change

358 when mode conversion occurs. Wavelength shift does not affect the received waves in the

359 numerical model because sensing can be done at just one point, but the EMAT is a finite

360 sized sensor with a spatial bandwidth [30]. Whilst the EMAT has a wide operating region, as

361 can be seen in Fig. 1, there is an effect on the experimental signals. In order to compare the

362 coefficients from experimental and simulated data, one also has to compensate for the effect

363 of wavelength shift on experimental data, or include its effects on the simulated data.

364 Including the spatial bandwidth in the simulation is more straightforward and robust, because

365 compensating for the wavelength shift in the experimental data would require deconvolution

366 of the experimental signal, accounting for the transducer's spatial profile and the wavelength

367 of the mode-converted wave, which can inherently introduce errors due to the low amplitude

17

368 of the raw data and subsequent overcompensation. Including the spatial bandwidth in the

369 simulation was done by simply convolving the simulated field with the theoretical probe

370 spatial profile, which is a 3 cycles spatial tone burst with a 10 mm period.

4.1. Experimental results for incident SH0 mode

372 Experimental coefficients for 90°, 45° and 10° defects as a function of the defect depth are

373 shown in Fig. 8 together with numerical coefficients showing very close agreement for non-

374 mode converted waves. When dealing with mode conversion, simulations and experiments

375 show less precise agreement, although all the coefficient's trends are the same in both

376 experiment and simulation. The less precise values related to mode-conversion are mainly

377 due to the wavelength shift effect, which was treated by including the probe spatial profile in

378 the simulated field. Nevertheless, differences still exist between the simplified tone burst

379 spatial profile adopted here and the exact one produced by the magnetic field due to the PPM

380 magnets array in the real probe. The coefficients for 90°, shown in Fig. 8 (a) and (b), agree

381 with those obtained numerically and theoretically calculated in [15]. A remark on the

382 experimental coefficient is necessary to clarify the fact that coefficient T_{01}, presents a trend to

383 increase for deeper defects, Fig. 8 (b), (d) and (f). This experimental artefact arises because

384 the raw signals received inside the defect present high amplitude because the SH0 waves are

385 very intense in this position, due to the energy concentration in the thinner region. Since these

386 raw signals are combined, following [29], in order to separate the mode-converted SH1

387 mode, then, any mode selectivity error in the experimental setup, which is intrinsically higher

388 on the selection of a wave arising from mode conversion, is increased in this case.
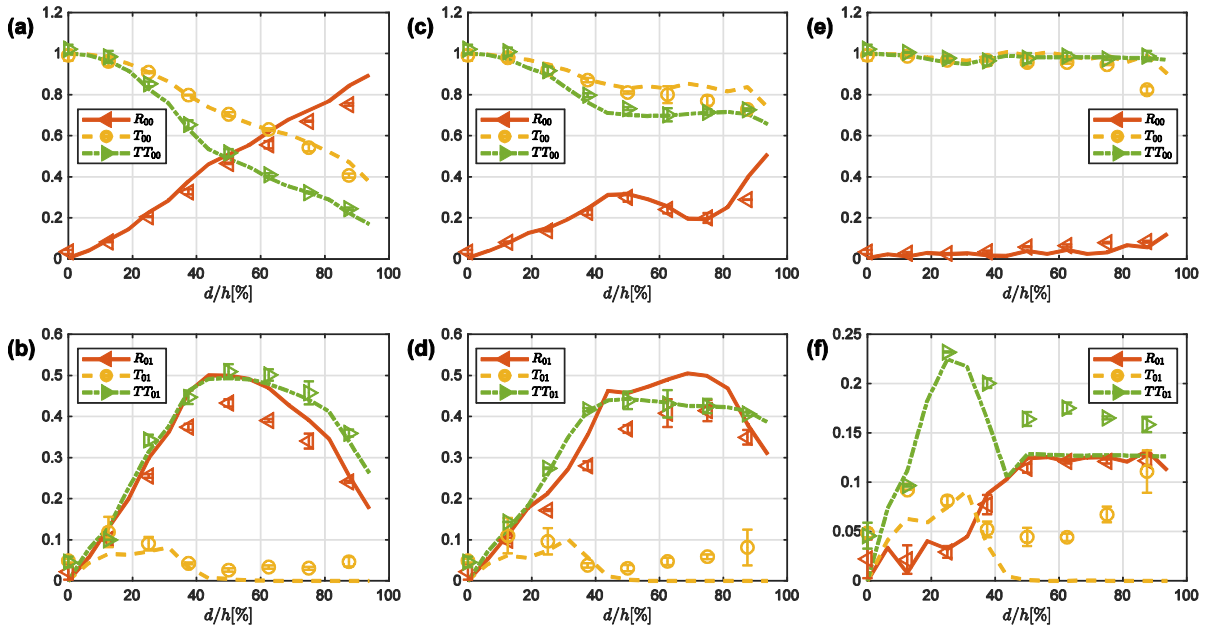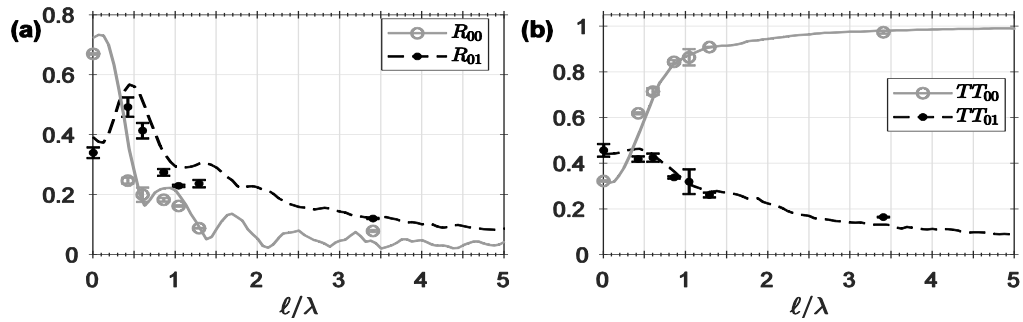
Fig.8. Experimental (symbols) and numerical (lines) coefficients for a SH0 generated at 90° defect (a) and (b), 45° (c) and (d) and 10° (e) and (f). Error bar denotes one standard deviation for repetitions of each experimental point, defect depth and edge angle, in the same specimen.

In order to verify non-monotonic characteristics for the coefficients, mainly for the reflection coefficient, a careful experimental investigation was undertaken for defect depths of 75% and 88% of plate thickness by machining additional plates with different edge angles. Fig. 9 and 10 show coefficients R_{0j} and TT_{0j} for defect depths of 25% and 75% of plate thickness as a function of the taper length. There is a clear non-monotonic characteristic for the coefficients obtained in finite element simulations, particularly for the reflection coefficient. For shallow defects (d/h $\leq$25%), the distribution of peaks and valleys of the reflection coefficient of R_{00} and R_{01} are approximately the same, whereas, for deep defects, the taper length in which a maximum of R_{00} occurs is the taper length in which a minimum of R_{01} occurs, and vice versa. As shown in Fig.10, the strong non-monotonic and oscillatory behaviour for deep defect depths are clearly confirmed by experimental measurements with reasonable agreement with the numerical simulations.
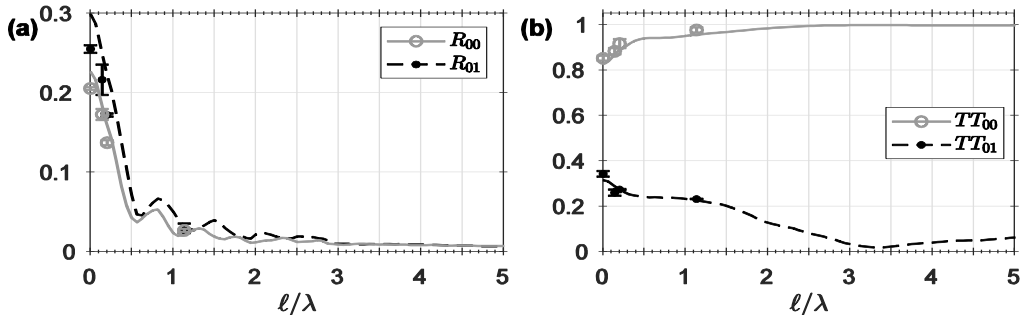
Fig.9. Experimental (symbols) and numerical (lines) coefficients R_{0j} (a) and TT_{0j} (b) for a defect with a depth equal to 25% of the plate thickness as a function of the taper length.

Fig.10. Experimental (symbols) and numerical (lines) coefficients R_{0j} (a) and TT_{0j} (b) for a defect with a depth equal to 75% of the plate thickness as a function of the taper length.

4.2. Experimental results for incident SH1 mode

Similar experiments were done for generation of the SH1 mode. Fig. 11 shows all the coefficients for increasing thinner region depth at 90°, 55° and 10° fixed angles obtained through numerical and experimental analysis.
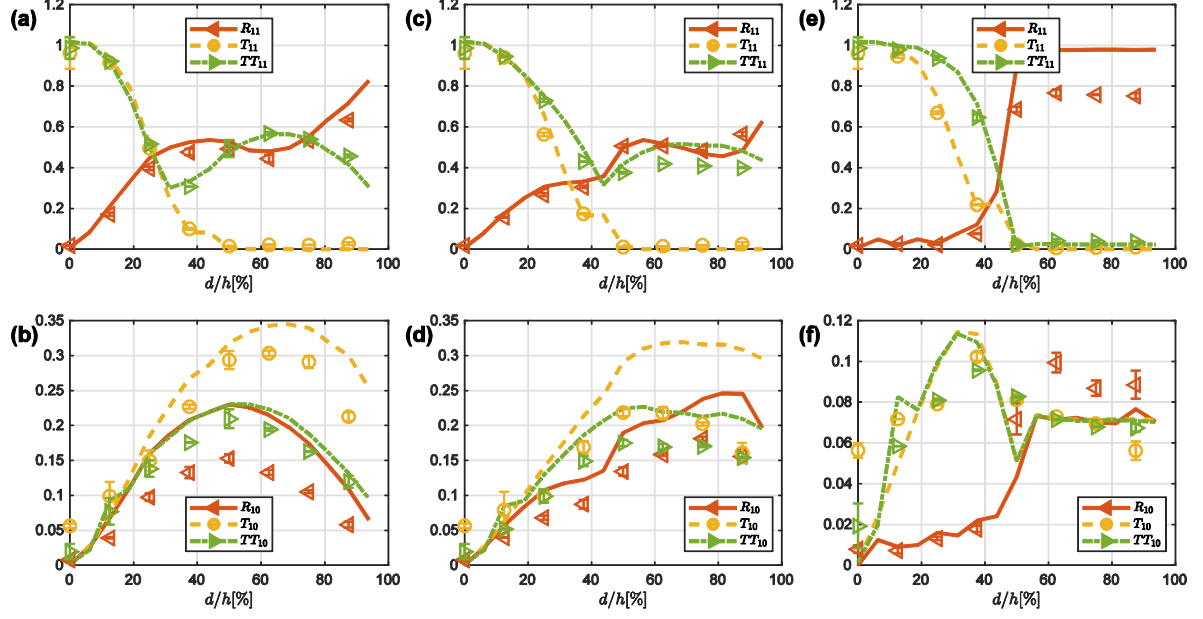
Fig.11. Experimental (symbols) and numerical (lines) coefficients for a SH1 generated at 90° defect (a) and (b), 55° (c) and (d), and 10° (e) and (f). Error bar denotes one standard deviation for repetitions of each experimental point, defect depth and edge angle, in the same specimen.

The coefficients R_{1j} and TT_{1j} for the defect region of 25%, 75% and 88% depths are shown in Fig. 12 to 14 as a function of the taper length. It is clearly seen that for shallow defects, R_{11} and R_{10} decrease as the taper increases but in a non-monotonic way, presenting maxima and minima. When the thinned region is thicker than the cut-off thickness of the SH1 mode, total transmission is obtained for long tapers, i.e. $R_{11} \to 0$ and $TT_{11} \to 1$ as $\ell \to \infty$. For thinned regions with a thickness less than the cut-off thickness, total reflection occurs, i.e. $R_{11} \to 1$ and $TT_{11} \to 0$ as $\ell \to \infty$. This means that the SH1 mode tends to be totally reflected with no mode conversion. The results show highly non-monotonic behaviour. For d/h = 75% and 88%, Figs. 13 and 14, a very sharp dip in R_{11} is found for taper length below half of the wavelength, then R_{11} increases. At the same taper length, there is a maximum in the coefficient TT_{11}.

430

Fig.12. Experimental (symbols) and numerical (lines) coefficients R_{1j} (a) and TT_{1j} (b) for a defect with a depth

equal to 25% of the plate thickness as a function of the taper length

433

Fig.13. Experimental (symbols) and numerical (lines) coefficients R_{1j} (a) and TT_{1j} (b) for a defect with a depth

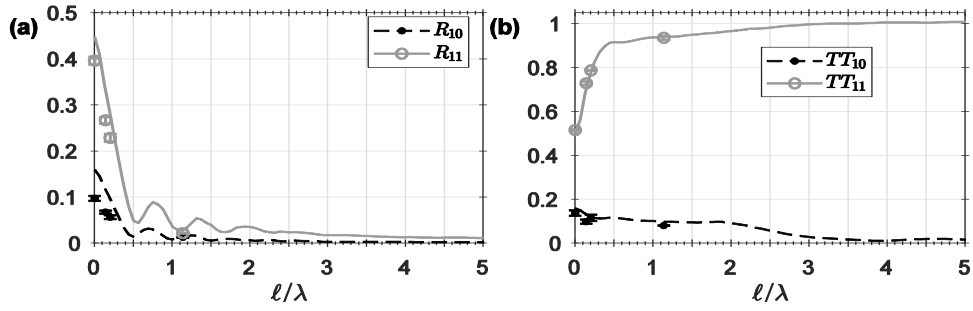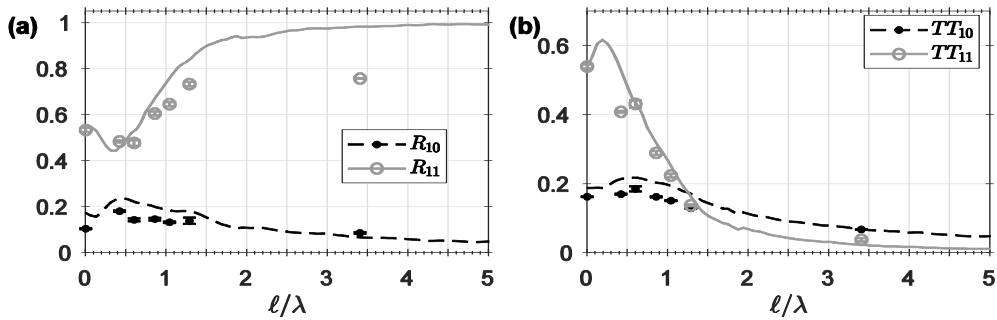equal to 75% of the plate thickness as a function of the taper length.

436
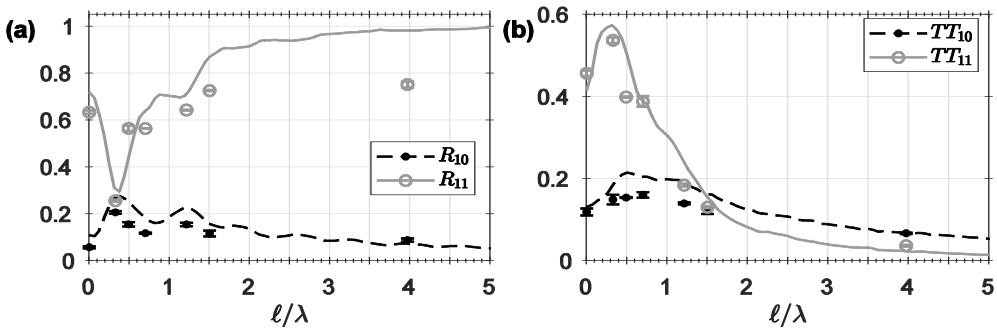
Fig.14. Experimental (symbols) and numerical (lines) coefficients R_{1j} (a) and TT_{1j} (b) for a defect with a depth

equal to 88% of the plate thickness as a function of the taper length.

5. Discussion

The extensive investigation described in this paper has made it possible to observe some

interesting and non-intuitive behaviour, regarding the interaction of SH guided wave modes

with wall thinning regions simulating wall loss due to corrosion. It was confirmed that the

22

443   taper length from the original thickness to the thinned region of the plate dictates the

444   reflection and transmission coefficients at both edges of the defect region and the level of

445   mode conversion, as previous work reported [3, 8, 18, 19, 24, 25]. For very long tapers, there

446   is no mode conversion and the behaviour is relatively simple, there is either total transmission

447   or total reflection. However, as the taper length decreases, the interaction becomes much

448   more unpredictable than was previously suggested in earlier work [3, 8, 18, 19, 24, 25]. This

449   paper rigorously demonstrates that reflection and transmission of SH guided waves through

450   even the simplified defect model adopted here is not monotonic, either regarding defect depth

451   or the edge angle.

452   The observed coefficients' behaviour is due to the interaction of the modes at both ends of

453   the taper as well as along its length. At the low thickness-frequency regime the periodical

454   oscillation pattern for the reflection coefficients as a function of the taper length was

455   attributed to the interference of the reflected waves at the two ends of the taper, since no

456   reflection of the fundamental mode occurred within the taper, uniquely at the taper's ends

457   [13]. This interference phenomenon is still somehow relevant for the SH0 here, since the

458   periodical pattern still holds, with the same distributions of maxima and minima for shallow

459   defects. The SH1 mode, on the other hand, does not necessarily reflect at the taper's end;

460   when the remaining thickness is less than its cut-off thickness, the SH1 mode has to reflect, at

461   the most, at the longitudinal position whose thickness is equal to its cut-off thickness, instead

462   of at the taper's end, as also observed by Nurmalia et al. [18]. Since this farthest reflection

463   position depends on the taper length, the SH1 mode's coefficient cannot follow the same

464   periodicity versus the taper length as the SH0 mode does.

465   However, in the high thickness-frequency regime, the overall mechanism is yet more

466   complex and depends on other interference factors. When a new mode is converted it may

467   undergo successive reflections and mode conversions not only at its ends but also within the

468 taper, all of which contributes to the resulting reflected or transmitted modes. Fig. 15 shows a

469 numerical example of the wave fields for SH0 and SH1 around the leading edge of a 6mm

470 deep thinning region with about $\ell = 1.5\lambda$ taper length when the SH1 mode was generated; a

471 considerable long taper was chosen in order to ease visualization along the taper length. The

472 separated fields for the SH0 and SH1 modes are shown in Fig. 15 (a) and (b), respectively.

473 One can observe that the incoming SH1 is progressively converted to the SH0, from the taper

474 start point, marked with a dotted arrow in Fig. 15(a), until the position where taper thickness

475 reaches its cut-off thickness where it is strongly converted to the SH0 mode and reflected

476 back as the SH1 mode, marked with dashed arrows in Fig.15(a) and (b), respectively; recall

477 that the SH1 mode cannot propagate further due to the low thickness. Additional low

478 amplitude reflections are also noticeable for the converted SH0, marked with dashed arrows

479 in Fig.15 (a), which in turns leads to successive interference. Similar reflections do occur for

480 the SH1, however, their amplitudes are considerably lower than the main SH1 beam to be

481 noticed in Fig.15(b). Therefore, the resulting intensity of the SH modes seen away from the

482 defect's edge is due to the non-trivial interaction of the modes in the taper region which

483 yields to the peculiar coefficient values along the defect depth and taper length ranges.
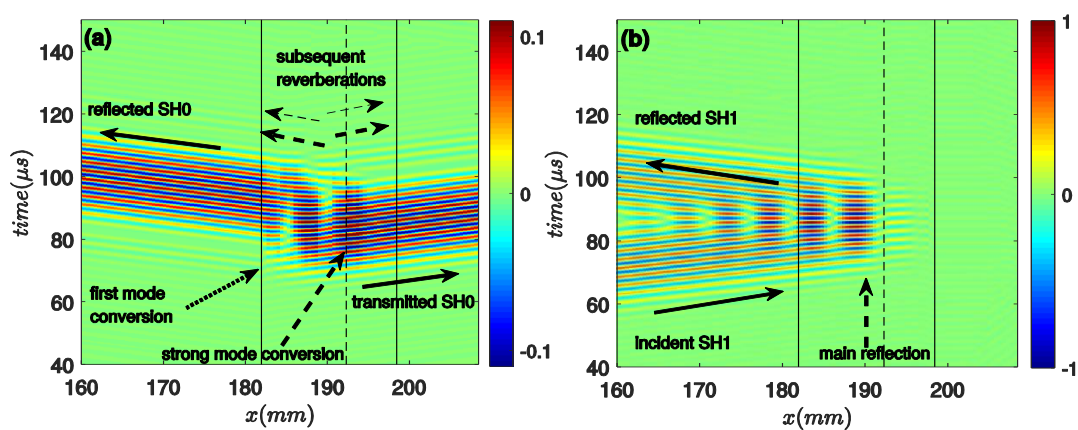
484

485 Fig.15. Interaction of incident SH1 mode with a 6mm deep defect at 20° edges. Normalized particle velocity

486 field for (a) SH0 and (b) SH1 modes. Continuous vertical lines denote the taper start and end positions, dashed

487 vertical lines denote the position where the SH1 mode cut-off thickness is found.

24

488   Concerning the use of SH guided waves for non-destructive evaluation of corroded plates

489   and pipes [3, 9, 26], this results highlight that the interaction is quite complex and for

490   instance the use of baseline signals obtained in a machined specimen with the most common,

491   and easy to machine, rectangular cross section [2, 10, 11, 14] will not reproduce the

492   phenomenon happening in real corrosion defects. Similar conclusions have been reached in

493   simpler cases, in which no mode conversion was possible [13, 20, 21]. Nevertheless, the

494   effect when mode conversion is possible is even more complicated and strongly dependent on

495   the defect shape. For instance, the reflection of the converted mode can be higher or lower

496   than in a specimen with a rectangular shape defect, if the real defect presents its edges with

497   intermediate or lower angles, respectively. It is also worth noticing that the presence of a

498   transmitted SH1 mode throughout a thinner region does not indicate the absence of a deep

499   defect. In the case of a deep, but abrupt defect (90° edges), the SH1 mode is detected with

500   significant amplitude; and with higher amplitudes when the taper length is approximately one

501   quarter wavelength, as shown in Figs. 13 and 14. Therefore, since the thinning rate of real

502   corrosion defects is generally unknown, the use of the presence or absence of a through

503   transmitted SH1 mode in order to identify a deep defect, as has been employed elsewhere [9,

504   26] is limited.

505   Additionally, quantification of defect depth through the intensity of either the reflected or

506   transmitted waves, using converted or non-mode converted waves would be complicated. It is

507   relevant to highlight that, a tapered wall thinning is a more relevant model for corrosion

508   defect than abrupt thickness reduction, but it is still not a completely realistic descriptive of a

509   corrosion defect shape, which may produce even more complex behaviour, and consequently,

510   quantification of defect geometry could be yet more complicated. For this reason, it would be

511   preferable to work on the low frequency-thickness regime [10, 13]. However, depending on

512   the plate or pipe thickness, this may be unfeasible or impose some very restrictive operating

513   conditions. For instance, in thick plates, the low-frequency regime requires very low

514   frequency guided waves, which implies not only poor time resolution, but will also require

515   long wavelengths, which in turn requires very large PPM EMATs to generate and receive the

516   waves. Nevertheless, alternative approaches for precise defect sizing could be attempted,

517   such as a non-linear multivariable inversion approach based on the set of reflection and

518   transmission coefficients for converted and non-converted modes calculated here. A similar

519   idea was used in order to size specific defect shapes in plates by means of both fundamental

520   Lamb wave modes [32, 33]. This technique has, however, to be restricted to an area that is

521   likely to contain the defect, in order to properly identify if the received signals come from a

522   reflected or a transmitted wave. It is also important to stress that this approach is very

523   restrictive on the defect shape under consideration; therefore further assessments on inferring

524   real corrosion defects through coefficients of tapered edge defect model is necessary.

525   **6.   Conclusions**

526   The interaction of the fundamental and first-order shear horizontal guided wave modes

527   with wall thinning with different depths and taper length in plates was experimentally and

528   numerically investigated and the reflection and transmission coefficients were calculated. A

529   vast range of experimental measurements and finite element modelling were performed and

530   good correlation was achieved.

531   The reflection and transmission characteristics of SH guided waves with the most simple

532   corrosion-like defects, simulated here, depend on the degree of wall thinning and the length

533   of the taper. There are complex interference effects that can occur on entering or exiting a

534   defect region and within the defect region itself, where remaining wall thickness and length

535   of defect have an effect on transmission and reflection of SH guided waves. These

536   characteristics make the reflection and transmission of either converted or non-converted

536 modes to be complex and non-monotonic along the taper length or thinning depth. This

538 would suggest that the use of SH guided waves, in the high frequency-thickness regime, for

539 detailed profiling of real corrosion defects, which may produce even more complex

540 behaviour, is complicated, being, thus, best suited to screening type approaches in NDT.

541

545 **References**

546 [1] P. Rajagopal and M. J. S. Lowe, "Scattering of the fundamental shear horizontal guided wave by a part-
547   thickness crack in an isotropic plate," *The Journal of the Acoustical Society of America,* vol. 124, no. 5,
548   pp. 2895-2904, 2008.
549 [2] A. Demma, P. Cawley, M. Lowe, A. G. Roosenbrand, and B. Pavlakovic, "The reflection of guided
550   waves from notches in pipes: a guide for interpreting corrosion measurements," *NDT & E*
551   *International,* vol. 37, no. 3, pp. 167-180, 2004/04/01/ 2004.
552 [3] M. Clough, M. Fleming, and S. Dixon, "Circumferential guided wave EMAT system for pipeline
553   screening using shear horizontal ultrasound," vol. 86, pp. 20-27, 2017.
554 [4] S. Wang, S. Huang, W. Zhao, and Z. Wei, "3D modeling of circumferential SH guided waves in
555   pipeline for axial cracking detection in ILI tools," *Ultrasonics,* vol. 56, pp. 325-331, 2015/02/01/ 2015.
556 [5] R. Howard and F. Cegla, "On the probability of detecting wall thinning defects with dispersive
557   circumferential guided waves," vol. 86, pp. 73-82, 2017.
558 [6] R. Howard and F. Cegla, "Detectability of corrosion damage with circumferential guided waves in
559   reflection and transmission," *NDT & E International,* vol. 91, pp. 108-119, 2017/10/01/ 2017.
560 [7] H. W. Kim, Y. E. Kwon, J. K. Lee, and Y. Y. Kim, "Higher torsional mode suppression in a pipe for
561   enhancing the first torsional mode by using magnetostrictive patch transducers," *IEEE Transactions on*
562   *Ultrasonics, Ferroelectrics, and Frequency Control,* vol. 60, no. 3, pp. 562-572, 2013.
563 [8] Y. E. Kwon, H. W. Kim, and Y. Y. Kim, "High-frequency lowest torsional wave mode ultrasonic
564   inspection using a necked pipe waveguide unit," *Ultrasonics,* vol. 62, pp. 237-243, 2015/09/01/ 2015.
565 [9] M. Hirao and H. Ogi, "An SH-wave EMAT technique for gas pipeline inspection," *NDT & E*
566   *International,* vol. 32, no. 3, pp. 127-132, 1999/04/01/ 1999.
567 [10] A. Demma, P. Cawley, and M. Lowe, "Scattering of the fundamental shear horizontal mode from steps
568   and notches in plates," *The Journal of the Acoustical Society of America,* vol. 113, no. 4, pp. 1880-
569   1891, 2003.
570 [11] A. Demma, P. Cawley, M. Lowe, and A. G. Roosenbrand, "The reflection of the fundamental torsional
571   mode from cracks and notches in pipes," *The Journal of the Acoustical Society of America,* vol. 114,
572   no. 2, pp. 611-625, 2003.
573 [12] J. Ma and P. Cawley, "Low-frequency pulse echo reflection of the fundamental shear horizontal mode
574   from part-thickness elliptical defects in plates," (in eng), *J Acoust Soc Am,* vol. 127, no. 6, pp. 3485-93,
575   Jun 2010.
576 [13] R. Carandente, J. Ma, and P. Cawley, "The scattering of the fundamental torsional mode from axi-
577   symmetric defects with varying depth profile in pipes," (in eng), *J Acoust Soc Am,* vol. 127, no. 6, pp.
578   3440-8, Jun 2010.
579 [14] H. Nurmalia and Nobutomo Nakamura and Hirotsugu Ogi and Masahiko, "Detection of Shear
580   Horizontal Guided Waves Propagating in Aluminum Plate with Thinning Region," *Japanese Journal of*
581   *Applied Physics,* vol. 50, no. 7S, p. 07HC17, 2011.

582 [15] A. Pau, D. V. Achillopoulou, and F. Vestroni, "Scattering of guided shear waves in plates with
583   discontinuities," *NDT & E International,* vol. 84, pp. 67-75, 2016/12/01/ 2016.
584 [16] A. Pau and D. V. Achillopoulou, "Interaction of Shear and Rayleigh-Lamb Waves with Notches and
585   Voids in Plate Waveguides," (in eng), *Materials (Basel),* vol. 10, no. 7, Jul 2017.
586 [17] P. Khalili and P. Cawley, "Relative Ability of Wedge-Coupled Piezoelectric and Meander Coil EMAT
587   Probes to Generate Single-Mode Lamb Waves," *IEEE Transactions on Ultrasonics, Ferroelectrics,
588   and Frequency Control,* vol. 65, no. 4, pp. 648-656, 2018.
589 [18] Nurmalia, N. Nakamura, H. Ogi, M. Hirao, and K. Nakahata, "Mode conversion behavior of SH guided
590   wave in a tapered plate," vol. 45, no. 1, pp. 156-161, 2012.
591 [19] H. Nurmalia and Nobutomo Nakamura and Hirotsugu Ogi and Masahiko, "Mode Conversion and Total
592   Reflection of Torsional Waves for Pipe Inspection," *Japanese Journal of Applied Physics,* vol. 52, no.
593   7S, p. 07HC14, 2013.
594 [20] R. Carandente, A. Lovstad, and P. Cawley, "The influence of sharp edges in corrosion profiles on the
595   reflection of guided waves," *NDT & E International,* vol. 52, pp. 57-68, 2012/11/01/ 2012.
596 [21] R. Carandente and P. Cawley, "The effect of complex defect profiles on the reflection of the
597   fundamental torsional mode in pipes," *NDT & E International,* vol. 46, pp. 41-47, 2012/03/01/ 2012.
598 [22] M. Koshiba, K. Hasegawa, and M. Suzuki, "Finite-Element Solution of Horizontally Polarized Shear
599   Wave Scattering in an Elastic Plate," *IEEE Transactions on Ultrasonics, Ferroelectrics, and
600   Frequency Control,* vol. 34, no. 4, pp. 461-466, 1987.
601 [23] J. J. Ditri, "Some results on the scattering of guided elastic SH waves from material and geometric
602   waveguide discontinuities," *The Journal of the Acoustical Society of America,* vol. 100, no. 5, pp.
603   3078-3087, 1996/11/01 1996.
604 [24] Y. E. Kwon, H. J. Jeon, H. W. Kim, and Y. Y. Kim, "Waveguide tapering for beam-width control in a
605   waveguide transducer," *Ultrasonics,* vol. 54, no. 3, pp. 953-960, 2014/03/01/ 2014.
606 [25] J.-J. Chen, G.-H. Song, and X. Han, "Asymmetric first order shear horizontal guided waves
607   propagation in a tapered plate," *Physics Letters A,* vol. 379, no. 36, pp. 2125-2129, 2015/09/25/ 2015.
608 [26] Nurmalia, N. Nakamura, H. Ogi, and M. Hirao, "EMAT pipe inspection technique using higher mode
609   torsional guided wave T(0,2)," *NDT & E International,* vol. 87, pp. 78-84, 2017/04/01/ 2017.
610 [27] J. L. Rose, *Ultrasonic Guided waves in solid media*. Cambridge University Press, 2014.
611 [28] P. A. Petcher and S. Dixon, "Mode mixing in shear horizontal ultrasonic guided waves,"
612   *Nondestructive Testing and Evaluation,* pp. 1-20, 2016.
613 [29] A. C. Kubrusly, M. A. Freitas, J. P. v. d. Weid, and S. Dixon, "Mode selectivity of SH guided waves by
614   dual excitation and reception applied to mode conversion analysis," *IEEE Transactions on Ultrasonics,
615   Ferroelectrics, and Frequency Control,* vol. 65, no. 7, pp. 1239 - 1249, 2018.
616 [30] S. Dixon, P. A. Petcher, Y. Fan, D. Maisey, and P. Nickolds, "Ultrasonic metal sheet thickness
617   measurement without prior wave speed calibration," *Journal of Physics D: Applied Physics,* vol. 46,
618   no. 44, p. 445502, 2013.
619 [31] P. A. Petcher, S. E. Burrows, and S. Dixon, "Shear horizontal (SH) ultrasound wave propagation
620   around smooth corners," vol. 54, no. 4, pp. 997-1004, 2014.
621 [32] M. Castaings, D. Singh, and P. Viot, "Sizing of impact damages in composite materials using
622   ultrasonic guided waves," *NDT & E International,* vol. 46, pp. 22-31, 2012/03/01/ 2012.
623 [33] D. Singh, M. Castaings, and C. Bacon, "Sizing strip-like defects in plates using guided waves," *NDT &
624   E International,* vol. 44, no. 5, pp. 394-404, 2011/09/01/ 2011.